

# La<sub>2</sub>SrCr<sub>2</sub>O<sub>7</sub>F<sub>2</sub>: A Ruddlesden–Popper Oxyfluoride Containing Octahedrally Coordinated Cr<sup>4+</sup> Centers

Ronghuan Zhang,<sup>†</sup> Gareth Read,<sup>†</sup> Franz Lang,<sup>‡</sup> Tom Lancaster,<sup>§</sup> Stephen J. Blundell,<sup>‡</sup> and Michael A. Hayward<sup>\*,†</sup>

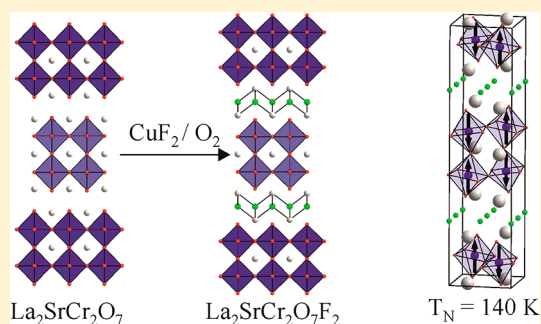
<sup>†</sup>Department of Chemistry, Inorganic Chemistry Laboratory, University of Oxford, South Parks Road, Oxford OX1 3QR, United Kingdom

<sup>‡</sup>Department of Physics, Clarendon Laboratory, University of Oxford, Parks Road, Oxford OX1 3PU, U.K.

<sup>§</sup>Department of Physics, Durham University, South Road, Durham DH1 3LE, U.K.

**S** Supporting Information

**ABSTRACT:** The low-temperature fluorination of the  $n = 2$  Ruddlesden–Popper phase La<sub>2</sub>SrCr<sub>2</sub>O<sub>7</sub> yields La<sub>2</sub>SrCr<sub>2</sub>O<sub>7</sub>F<sub>2</sub> via a topochemical fluorine insertion reaction. The structure-conserving nature of the fluorination reaction means that the chromium centers of the initial oxide phase retain an octahedral coordination environment in the fluorinated product, resulting in a material containing an extended array of apex-linked Cr<sup>4+</sup>O<sub>6</sub> units. Typically materials containing networks of octahedrally coordinated Cr<sup>4+</sup> centers can only be prepared at high pressure; thus, the preparation of La<sub>2</sub>SrCr<sub>2</sub>O<sub>7</sub>F<sub>2</sub> demonstrates that low-temperature topochemical reactions offer an alternative synthesis route to materials of this type. Neutron diffraction, magnetization, and  $\mu^+$ SR data indicate that La<sub>2</sub>SrCr<sub>2</sub>O<sub>7</sub>F<sub>2</sub> undergoes a transition to an antiferromagnetic state below  $T_N \approx 140$  K. The structure–property relations of this phase



and other Cr<sup>4+</sup> oxide phases are discussed.

## INTRODUCTION

There has been enduring interest in complex transition metal oxide phases due to the wide variety of unusual physical properties they exhibit. A particularly fruitful area for the discovery of novel physical behavior has been the investigation of phases which lie close to metal–insulator transitions, as these materials often play host to a number of different competing electronic ground states. As these ground states have similar stabilities, small chemical or structural modifications of such systems can be used to adjust the relative energies and thus stabilities of these competing states, enabling the properties of the materials to be tuned to potentially exhibit exotic behavior such as superconductivity or magnetoresistance.<sup>1</sup>

Cubic perovskite phases containing octahedrally coordinated Cr<sup>4+</sup> centers fall into this category of materials because the bandwidth  $W$ , arising from the overlap of chromium  $d$  orbitals, and the Hubbard  $U$ , arising from electron–electron interactions, are approximately equal; thus, small structural changes, such as adjusting the Cr–O–Cr bond angle of a phase, can be used to tune behavior from metallic to insulating. However, the study of Cr<sup>4+</sup>-containing perovskite phases is challenging, as the ionic radius of Cr<sup>4+</sup> is too small to readily occupy the 6-fold octahedral B-cation site in the perovskite lattice (4-fold tetrahedral coordination is preferred). This means that perovskite phases (and the related layered Ruddlesden–Popper phases) containing Cr<sup>4+</sup> can normally only be prepared under high-pressure conditions.<sup>2</sup> As a result, the samples produced

tend to be of small size and contain binary chromium oxide impurities, typically CrO<sub>2</sub>, which hamper the detailed physical characterization of these phases.<sup>2</sup>

The low-temperature topochemical modification of complex transition-metal oxides offers many opportunities for preparing metastable phases containing transition-metal centers with unusual oxidation state/coordination geometry combinations, because the reactions are performed under kinetic, rather than thermodynamic, control.<sup>3,4</sup> By adopting such an approach, it is possible to avoid the need to use high-pressure synthesis conditions to prepare extended oxide phases containing octahedrally coordinated Cr<sup>4+</sup> centers.

A particularly useful set of reactions in this regard are the oxidative anion insertion reactions of layered Ruddlesden–Popper oxides. For example, reaction of A<sub>3</sub>B<sub>2</sub>O<sub>7</sub>  $n = 2$  Ruddlesden–Popper oxides with fluorine gas or with *in situ* fluorine sources such as CuF<sub>2</sub> or poly(vinylidene fluoride) leads to the oxidative insertion of fluoride ions into vacant tetrahedral anion coordination sites within the “rock salt” layers of the materials, which in the simplest case convert the A<sub>3</sub>B<sub>2</sub>O<sub>7</sub> phase into an A<sub>3</sub>B<sub>2</sub>O<sub>7</sub>F<sub>2</sub> phase, as shown in Figure 1.<sup>5–7</sup> The insertion of fluoride ions raises the oxidation state of the B-cations by one unit, but because the fluoride ions are inserted into the structure outside the coordination sphere of the B-cations, their

Received: January 15, 2016

Published: March 9, 2016

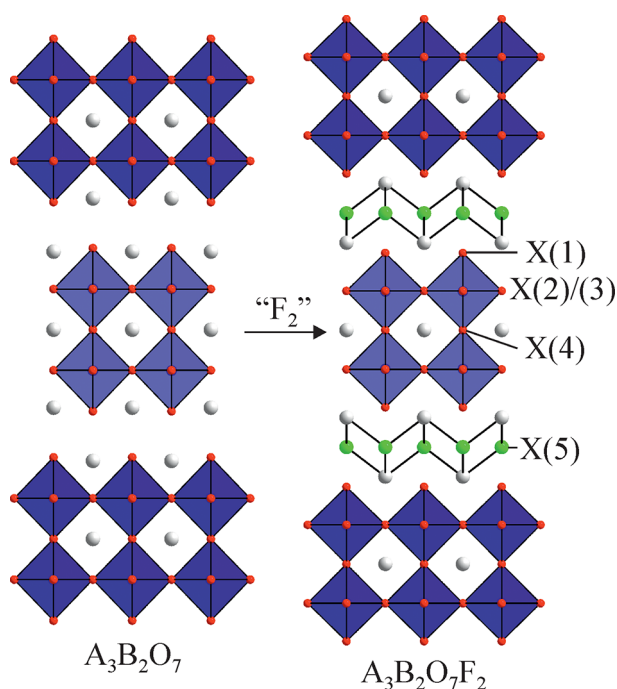


**Figure 1.** Reaction of  $A_3B_2O_7$ ,  $n = 2$  Ruddlesden–Popper phases with fluorine, bringing about the topochemical, oxidative insertion of fluorine and the formation of the related  $A_3B_2O_7F_2$  materials.<sup>5,6</sup>

local coordination geometry remains largely unchanged. Thus, we would expect that this type of topochemical fluorination performed on an  $A_3Cr^{3+}_2O_7$  phase should result in the formation of an  $A_3Cr^{4+}_2O_7F_2$  phase containing sheets of apex-linked, octahedrally coordinated  $Cr^{4+}$  centers.

Here we describe the fluorination and subsequent characterization of  $La_2SrCr_2O_7$ , a  $Cr^{3+}$ -containing  $n = 2$  Ruddlesden–Popper phase, prepared recently for this specific reason.<sup>8</sup>

## EXPERIMENTAL SECTION

**Synthesis.** Samples of  $La_2SrCr_2O_7$  were prepared as described elsewhere.<sup>8</sup> Suitable quantities of  $La_2O_3$  (99.999%, dried at 900 °C),  $SrCO_3$  (99.99%), and  $Cr_2O_3$  (99.97%) were ground together and then heated in air at 1000 °C for 20 h to decompose the carbonate. The resulting material was then pressed into 13 mm diameter pellets and heated at 1460 °C for four periods of 55 h under flowing argon. X-ray powder diffraction data collected from  $La_2SrCr_2O_7$  could be readily indexed using a monoclinic unit cell with  $a = 5.491$  Å,  $b = 5.479$  Å,  $c = 20.181$  Å, and  $\beta = 89.78^\circ$ , in good agreement with previously analyzed samples.<sup>8</sup>

Fluorination of  $La_2SrCr_2O_7$  was performed using  $CuF_2$  as a soft fluorination agent.<sup>6</sup> Typically  $CuF_2$  is used as an in situ fluorine source which is mixed with the material to be fluorinated and converted into  $CuO$  during the reaction, according to eq 1, resulting in the inevitable contamination of samples by  $CuO$ .



To avoid this contamination, we have developed a process where  $CuF_2$  is heated separately at 500 °C under flowing oxygen, to liberate fluorine, and the resulting mixture of gases is then passed over the material to be fluorinated, as we have described in detail previously.<sup>9</sup> Thus,  $La_2SrCr_2O_7$  was fluorinated by multiple heatings at 310 °C under the  $O_2/F_2$  gas mixture until the reaction was deemed complete by X-ray powder diffraction.

**Characterization.** X-ray powder diffraction data were collected using a PANalytical X'pert diffractometer incorporating an X'celerator position-sensitive detector (monochromatic  $Cu\ K\alpha_1$  radiation).

Neutron powder diffraction data were collected using the GEM diffractometer at the ISIS neutron source in the U.K., from samples contained in cylindrical vanadium cans. Rietveld profile refinements were performed using the GSAS suite of programs.<sup>10</sup> Thermogravimetric reduction measurements were performed by heating powder samples under a 10%  $H_2$  in  $N_2$  atmosphere using a Mettler-Toledo MX1 thermogravimetric microbalance. Magnetization data were collected from powder samples using a Quantum Design MPMS SQUID magnetometer in an applied field of 100 Oe. The  $\mu^+SR$  experiments were carried out at the Swiss Muon Source, PSI, in Switzerland. In a  $\mu^+SR$  experiment, spin-polarized muons were implanted in the bulk of a material and the time dependence of their polarization was monitored by recording the angular distribution of the subsequent positron decay.

## RESULTS

**Fluorination Chemistry of  $La_2SrCr_2O_7$ .** Heating samples of  $La_2SrCr_2O_7$  at 310 °C under an  $F_2/O_2$  gas flow, as described above, yields a black material and led to an expansion of the  $c$  lattice parameter of the phase, as determined by powder X-ray diffraction, consistent with the topochemical insertion of fluorine. During the fluorination process the only phases observed by diffraction were the starting material and the “fully fluorinated” product phase, with no evidence of intermediate, partially fluorinated phases. Raising the reaction temperature above 310 °C led to the formation of poorly crystalline binary fluoride phases ( $SrF_2$ ,  $LaF_3$ ) consistent with nontopochemical decomposition reactions. It should be noted that heating samples of  $La_2SrCr_2O_7$  under a pure oxygen flow at 310 °C in the absence of  $CuF_2$  led to no observable reaction.

**Compositional Characterization of  $La_2SrCr_2O_7F_2$ .** Attempts to determine the composition of the product of fluorination of  $La_2SrCr_2O_7$  via iodometric titration proved ineffective, as the fluorinated phase was insoluble. As an alternative, fluorinated samples were heated to 800 °C under a flowing 10%  $H_2/N_2$  atmosphere on a TGA microbalance. X-ray powder diffraction data collected from samples heated in this way indicated that the sample had been converted to a mixture of  $SrF_2$  and  $LaCrO_3$  (Figure S1 in the Supporting Information). In combination with the observed mass loss (2.46%, Figure S2 in the Supporting Information) and the structural analysis described below, this is consistent with a composition of  $La_2SrCr_2O_7F_2$  for the fluorinated sample.

**Structural Refinement of  $La_2SrCr_2O_7F_2$ .** Neutron powder diffraction data collected from a fluorinated sample of  $La_2SrCr_2O_7$ , henceforth referred to as  $La_2SrCr_2O_7F_2$ , could be indexed using a monoclinic unit cell ( $a = 5.426$  Å,  $b = 5.468$  Å,  $c = 22.682$  Å,  $\beta = 90.4^\circ$ ) with extinction conditions consistent with A-centering. A model based on the structures of fluorine-inserted  $Sr_3M_2O_7F_2$  Ruddlesden–Popper phases<sup>5,6</sup> was constructed in space group  $A2/a$  and refined against the diffraction data. During the refinement the La/Sr A-cation distribution was fixed at the values observed for the  $La_2SrCr_2O_7$  parent phase,<sup>8</sup> with all other atomic positional and displacement parameters allowed to refine freely. Given the similarity of the neutron scattering lengths of oxygen and fluorine (O, 5.80 fm; F, 5.65 fm)<sup>11</sup> no attempt was made to determine the anion distribution at this stage, and all the anion sites were occupied by oxygen within the model. Refinement of the anion site occupancies indicated that all the anion sites were fully occupied, within error. In common with the all-oxide parent phase, the diffraction data collected from  $La_2SrCr_2O_7F_2$  exhibited weak  $hkl$  dependent peak broadening; therefore, an anisotropic broadening axis (001) was added to the peak shape description

**Table 1.** Structural Parameters Refined against Neutron Powder Diffraction Data Collected at 300 K from  $\text{La}_2\text{SrCr}_2\text{O}_7\text{F}_2^a$ 

	x	y	z	fraction	$U_{\text{iso}}$ ( $\text{\AA}^2$ )
La/Sr(1)	1/4	0.7525(10)	0	0.82/0.17	0.0045(6)
La/Sr(2)	0.2516(7)	0.7507(7)	0.1787(1)	0.58/0.42	0.0065(5)
Cr(1)	0.2474(18)	0.2501(14)	0.0848(2)	1	0.0016(5)
O(1)	0.2584(10)	0.2920(8)	0.1655(1)	1	0.0093(7)
O(2)	1/4	0.2107(14)	0	1	0.0130(10)
O(3)	0.9689(8)	0.0300(10)	0.0936(1)	1	0.0062(8)
O(4)	0.5256(9)	0.4759(12)	0.0758(1)	1	0.0061(8)
F(1)	0.4957(7)	0.5004(13)	0.2517(1)	1	0.0082(5)

<sup>a</sup> $\text{La}_2\text{SrCr}_2\text{O}_7\text{F}_2$ : space group  $A2/a$ ,  $a = 5.4262(6)$   $\text{\AA}$ ,  $b = 5.4681(7)$   $\text{\AA}$ ,  $c = 22.682(2)$   $\text{\AA}$ ,  $\beta = 90.44(1)^\circ$ ,  $V = 672.9(2)\text{\AA}^3$ , phase fraction 96.7(1) wt %.  $\text{LaCrO}_3$ : space group  $Pnma$ ,  $a = 5.467(2)$   $\text{\AA}$ ,  $b = 7.764(5)$   $\text{\AA}$ ,  $c = 5.513(2)$   $\text{\AA}$ , phase fraction 3.4(1) wt %.  $\chi^2 = 5.34$ ,  $R_{\text{wp}} = 4.45\%$ ,  $R_p = 3.79\%$ .

to allow crystal microstrain perpendicular and parallel to this axis to be refined independently. In addition, features attributable a small amount of  $\text{LaCrO}_3$  in the sample were observed; therefore, a second phase was added to the structural model to account for these. The refinement converged smoothly to give a good statistical fit; details of the refined structure of  $\text{La}_2\text{SrCr}_2\text{O}_7\text{F}_2$  are given in Table 1 with selected bond lengths in Table 2. Plots of the observed and calculated

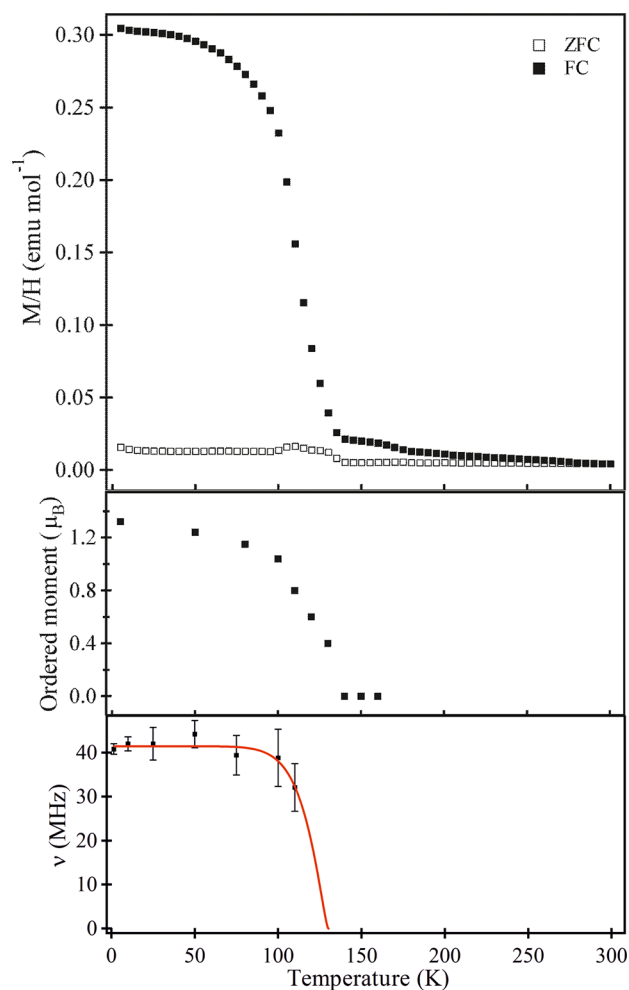
**Table 2.** Selected Bond Lengths and Angles and Bond Valence Sums from the Refined Structure of  $\text{La}_2\text{SrCr}_2\text{O}_7\text{F}_2$  at 298 K

cation	anion	bond length ( $\text{\AA}$ )	BVS		
La/Sr(1)	O(2)	2.505(9)	La +3.026/Sr +2.615		
	O(2)	2.721(1) $\times 2$			
	O(2)	2.963(9)			
	O(3)	2.701(10) $\times 2$			
	O(3)	3.031(12) $\times 2$			
	O(4)	2.456(10) $\times 2$			
	O(4)	2.728(11) $\times 2$			
	La/Sr(2)	O(1)		2.526(6)	La +2.790/Sr +2.455
		O(1)		2.701(7)	
		O(1)		2.778(7)	
O(1)		2.975(6)			
O(3)		2.567(10)			
O(3)		2.892(11)			
O(4)		2.906(11)			
O(4)		3.157(12)			
F(1)		2.488(10) $\times 2$			
F(1)		2.567(11)			
Cr(1)	F(1)	2.517(10)	Cr +3.467		
	O(1)	1.845(5)			
	O(2)	1.936(5)			
	O(3)	1.943(10)			
	O(3)	1.956(10)			
	O(4)	1.932(10)			
	O(4)	1.962(11)			
				angle (deg)	
	Cr(1)–O(2)–Cr(1)	167.2(1)			
	Cr(1)–O(3)–Cr(1)	162.1(4)			
	Cr(1)–O(4)–Cr(1)	163.0(4)			

data are shown in Figure S3 in the Supporting Information. Analysis of the bond valence sums (BVS)<sup>12</sup> of the different anion sites in the structure of  $\text{La}_2\text{SrCr}_2\text{O}_7\text{F}_2$  (described in detail in the Discussion) reveals that, in common with many previously reported  $\text{A}_3\text{B}_2\text{O}_7\text{F}_2$  phases,<sup>5,6</sup> the fluoride ions in  $\text{La}_2\text{SrCr}_2\text{O}_7\text{F}_2$  are located on the new interstitial anion sites

located within the rock salt layers of the material and are therefore described in this way in Table 1.

**Magnetic Characterization of  $\text{La}_2\text{SrCr}_2\text{O}_7\text{F}_2$ .** Magnetization data collected from  $\text{La}_2\text{SrCr}_2\text{O}_7\text{F}_2$  in an applied field of 100 Oe show a divergence between zero-field-cooled and field-cooled data below 280 K (which corresponds to the magnetic ordering temperature of the  $\text{La}_2\text{SrCr}_2\text{O}_7$  starting material)<sup>8</sup> which increases dramatically below 140 K, as shown in Figure 2.

**Figure 2.** Plots of zero-field-cooled and field-cooled magnetization (top), ordered magnetic moment extracted from fits to neutron powder diffraction data (middle), and muon oscillation frequency (bottom) collected as a function of temperature from  $\text{La}_2\text{SrCr}_2\text{O}_7\text{F}_2$ .

Neutron powder diffraction data collected from  $\text{La}_2\text{SrCr}_2\text{O}_7\text{F}_2$  at 5 K show additional diffraction features in comparison to analogous data collected at 300 K, consistent with the presence of magnetic order at low temperature. The additional diffraction features can be indexed using the crystallographic unit cell, indicating the magnetic ordering vector  $\mathbf{k} = 0$ . A magnetic symmetry analysis using the SARAH code<sup>13</sup> was performed (space group  $A2/a$ ) to yield four irreducible representations each consisting of three basis vectors. These symmetry-compatible magnetic models were individually refined against the low-temperature neutron diffraction data, and it was observed that the magnetic diffraction intensity was best accounted for using the irreducible representation corresponding to Shubnikov group  $A2/a$ , which is a G-type antiferromagnetic model with spins aligned parallel to the crystallographic  $c$  axis, as shown in Figure 3. This

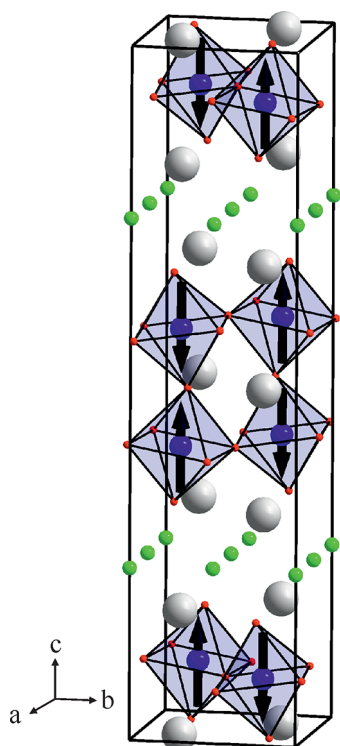


**Figure 3.** Magnetic structure of  $\text{La}_2\text{SrCr}_2\text{O}_7\text{F}_2$  refined from neutron powder diffraction collected at 5K. The ordered moment is  $1.32(2) \mu_B$  per chromium center at 5 K.

irreducible representation allows for weak ferromagnetism along the crystallographic  $b$  axis (consistent with the weak ferromagnetism observed in the magnetization data); however, this component of the magnetic lattice was too small to be extracted from the diffraction data and so was set to 0. A full description of the nuclear and magnetic structural refinement of  $\text{La}_2\text{SrCr}_2\text{O}_7\text{F}_2$  is given in Tables S3 and S4 in the Supporting Information, along with plots of the observed and calculated diffraction data (Figure S5 in the Supporting Information). Neutron diffraction data collected on warming the sample indicate that the ordered moment declines from a value of  $1.32(2) \mu_B$  per chromium center at 5 K to  $0 \mu_B$  at 140 K, as shown in Figure 2. The observed ordered moment at 5 K is smaller than what would be expected for a spin-only,  $S = 1$  center, suggesting an unquenched orbital contribution to the moment.

Zero-field  $\mu^+$ SR data were collected from  $\text{La}_2\text{SrCr}_2\text{O}_7\text{F}_2$  as a function of temperature. As shown in Figure S4 in the Supporting Information and Figure 2, strong persistent oscillations were observed in data collected at 5 K, consistent with long-range antiferromagnetic order. These oscillations declined in frequency with increasing temperature and ultimately disappeared from the signal at  $T \approx 140$  K, in agreement with the antiferromagnetic ordering temperatures observed in the magnetization and neutron diffraction data. A cold-pressed pellet of  $\text{La}_2\text{Sr}_2\text{Cr}_2\text{O}_7\text{F}_2$  had a resistivity at room temperature which was greater than what could be measured with our apparatus ( $\rho > 100 \text{ K}\Omega \text{ cm}$  @ 300 K), consistent with insulating behavior.

## DISCUSSION

**Anion Composition.** Thermogravimetric data, in combination with diffraction data, indicate that the fluorination of  $\text{La}_2\text{SrCr}_2\text{O}_7$  yields  $\text{La}_2\text{SrCr}_2\text{O}_7\text{F}_2$ . This fluorinated composition shows that the fluorination reaction proceeds via insertion of fluorine into the parent oxide phase without any anion exchange. Such behavior is somewhat unusual, because while  $\text{Sr}_3\text{RuMO}_7$  ( $M = \text{Ru}, \text{Mn}, \text{Ti}$ ) and  $\text{Ln}_{1.2}\text{Sr}_{1.8}\text{Mn}_2\text{O}_7$  react in a similar manner by simple fluorine insertion, many  $n = 2$  Ruddlesden–Popper phases incorporate some anion exchange in their fluorination reactions. For example, fluorination of  $\text{Sr}_3\text{RuFeO}_7$  yields  $\text{Sr}_3\text{RuFeO}_{5.5}\text{F}_{3.5}$ , while fluorination of  $\text{La}_2\text{BaFe}_2\text{O}_7$  yields  $\text{La}_2\text{BaFe}_2\text{O}_5\text{F}_4$  in reactions that lead to no net change in the iron oxidation state. In the case of  $\text{La}_2\text{SrCr}_2\text{O}_7$ , direct oxidation to  $\text{La}_2\text{SrCr}_2\text{O}_7\text{F}_2$  can be attributed to the relative stability of  $\text{Cr}^{4+}$  centers in extended oxide phases.

**Crystal Structure.** The structure of  $\text{La}_2\text{SrCr}_2\text{O}_7\text{F}_2$ , determined by refinement against neutron powder diffraction data, has an additional tetrahedral anion coordination site within the “rock salt” layers of the phase, in comparison to the  $\text{La}_2\text{SrCr}_2\text{O}_7$  parent phase, in common with other topochemically fluorinated  $n = 2$  Ruddlesden–Popper oxides. As noted above, the lack of X-ray or neutron scattering contrast between  $\text{O}^{2-}$  and  $\text{F}^-$  prevents the direct determination of the oxide/fluoride anion distribution from diffraction data. However, it is possible to deduce the oxide/fluoride distributions in some oxide fluoride phases by detailed examination of the local bonding at anion sites using bond valence sums (BVS).<sup>5,9,14</sup> Table 3 shows the bond valence sums for the five crystallo-

**Table 3.** Anion Bond Valence Sums from  $\text{La}_2\text{SrCr}_2\text{O}_7$  and  $\text{La}_2\text{SrCr}_2\text{O}_7\text{F}_2$

$\text{La}_2\text{SrCr}_2\text{O}_7$		$\text{La}_2\text{SrCr}_2\text{O}_7\text{F}_2$		
anion	BVS(O)	anion	BVS(O)	BVS(F)
O(1)	1.756	X(1)/O(1)	1.677	1.275
O(2)	1.890	X(2)/O(2)	2.105	1.615
O(3)	2.208	X(3)/O(3)	1.911	1.470
O(4)	2.180	X(4)/O(4)	1.989	1.528
		X(5)/F(1)	1.588	1.164

graphically distinct anion sites in the structure of  $\text{La}_2\text{SrCr}_2\text{O}_7\text{F}_2$ , calculated as if they were occupied by either oxide or fluoride ions, and those of the analogous anion sites in the  $\text{La}_2\text{SrCr}_2\text{O}_7$  parent phase calculated for oxide occupation. The anion labeling scheme is shown in Figure 1 (X labels) and Table 1 (O/F labels). These data clearly show that the BVS of the additional anion site (X(5)/F(1)) is the smallest of all the anion sites in the phase, with values consistent with the

occupation of fluoride rather than oxide. This is further supported by the observation that the La/Sr(2)–F(1) bond lengths range from 2.48 to 2.56 Å, which is very similar to the Sr–F bond length observed for SrF<sub>2</sub> (2.511 Å)<sup>15</sup> and the range of M–F bond lengths seen in other fluorine intercalated Ruddlesden–Popper phases.<sup>5,6</sup> Furthermore, the La/Sr(2)–F(1) bond lengths are much longer than would be expected for an La/Sr–O bond. Thus, given that we know the composition of the phase is La<sub>2</sub>SrCr<sub>2</sub>O<sub>7</sub>F<sub>2</sub> and that the X(5) anion site is suitable for fluorine, but not for oxygen, we can conclude that, in common with Sr<sub>3</sub>(Ru<sub>0.5</sub>M<sub>0.5</sub>)<sub>2</sub>O<sub>7</sub> (M = Ru, Mn, Ti) phases, the fluorination of La<sub>2</sub>SrCr<sub>2</sub>O<sub>7</sub> occurs via the simple insertion of fluoride ions into the tetrahedral interstitial anion site within the phase.

An additional structural consequence of the fluoride insertion into La<sub>2</sub>SrCr<sub>2</sub>O<sub>7</sub> is a dramatic compression of the double-perovskite layers within the phase. While the *c* lattice parameter increases from 20.182 to 22.682 Å on fluorination, the *c* dimension of the double-perovskite blocks (measured as the distance parallel to the *z* axis between the axial O(1) anions) decreases from 7.99 to 7.50 Å, as shown in Figure 4. This

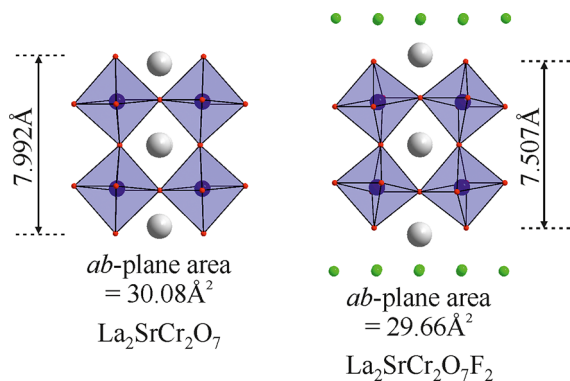


**Figure 4.** Fluorination of La<sub>2</sub>SrCr<sub>2</sub>O<sub>7</sub> leads to a compression of the perovskite blocks, both parallel to the *c* axis and in the *ab* plane, leading to a tightening of all Cr–O–Cr bond angles.

compression is greater than the contraction of the axial Cr–O bonds on oxidation, and in combination with the small contraction in the *ab* plane, this results in an increase in the size of the tilting and twisting distortions of the apex-linked CrO<sub>6</sub> octahedra on fluorination, such that the Cr–O–Cr bond angles contract from 170.8°, 175.0°, and 173.6° in La<sub>2</sub>SrCr<sub>2</sub>O<sub>7</sub><sup>8</sup> to 167.2°, 162.1°, and 163.0° in La<sub>2</sub>SrCr<sub>2</sub>O<sub>7</sub>F<sub>2</sub>, enhancing the cooperative tilting distortion (*a*<sup>–</sup>*a*<sup>–</sup>*c*<sup>–</sup> in Glazer notation<sup>16</sup>) of the perovskite double layers. The tightening of the Cr–O–Cr bond angles is slightly counterintuitive, as a more simple analysis might expect the tolerance factor, *t* ( $t = \langle A-O \rangle / (\sqrt{2} \langle B-O \rangle)$ ), to increase on oxidation of Cr<sup>3+</sup> to Cr<sup>4+</sup> and thus the Cr–O–Cr bond angles to approach 180°. However, it appears that the insertion of fluoride ions into the rock salt layers of the host phase leads to a contraction of the La/Sr–F sheets, which in combination with the increase in anion–anion repulsion on fluoride insertion overcomes the change in the tolerance factor, leading to a tightening of the bond angles, as has been observed previously in analogous fluorine insertion reactions.<sup>5</sup>

**Physical Behavior.** Neutron diffraction,  $\mu^+$ SR, and magnetization data reveal that La<sub>2</sub>SrCr<sub>2</sub>O<sub>7</sub>F<sub>2</sub> adopts a canted antiferromagnetic state below 140 K and is electronically insulating. Direct comparison of this behavior with other

Cr(IV) oxide phases which adopt perovskite or related structures is hampered by the presence of impurity phases in samples of these materials prepared at high pressure.<sup>2</sup> However, if the presence of impurities is taken into account, a survey of related phases reveals three suitable phases for comparison: Sr<sub>3</sub>Cr<sub>2</sub>O<sub>7</sub>, a structurally undistorted *n* = 2 Ruddlesden–Popper phase (space group *I4/mmm*, Cr–O–Cr = 180°) which is observed to be semiconducting, with antiferromagnetic order observed below 220 K;<sup>2</sup> CaCrO<sub>3</sub>, a structurally distorted perovskite phase (space group *Pnma*, Cr–O–Cr = 158.9, 157.7°) which exhibits antiferromagnetic order below 90 K;<sup>17,18</sup> SrCrO<sub>3</sub>, an undistorted perovskite phase (space group *Pm3m*, Cr–O–Cr = 180°) which has been described by different authors as either a paramagnetic phase with no sign of magnetic order down to 2 K<sup>19</sup> or as a phase which undergoes an orbital ordering transition and exhibiting antiferromagnetic order below *T*<sub>N</sub> ≈ 40 K,<sup>20</sup> the discrepancy presumably arising from the difficulty in preparing phase-pure, oxygen-stoichiometric samples.

At first sight the structure–property relations of these phases appear contradictory: structurally distorted CaCrO<sub>3</sub> has a higher magnetic ordering temperature than undistorted SrCrO<sub>3</sub>, yet structurally undistorted Sr<sub>3</sub>Cr<sub>2</sub>O<sub>7</sub> has a higher magnetic ordering temperature than distorted La<sub>2</sub>SrCr<sub>2</sub>O<sub>7</sub>F<sub>2</sub>. These apparently contradictory structure–property relationships can be rationalized by considering the analysis previously described by Goodenough which relates the magnetic ordering temperature of a phase to the strength of interaction between metal centers, quantified by the transfer integral *b*.<sup>17,21</sup> Figure 5

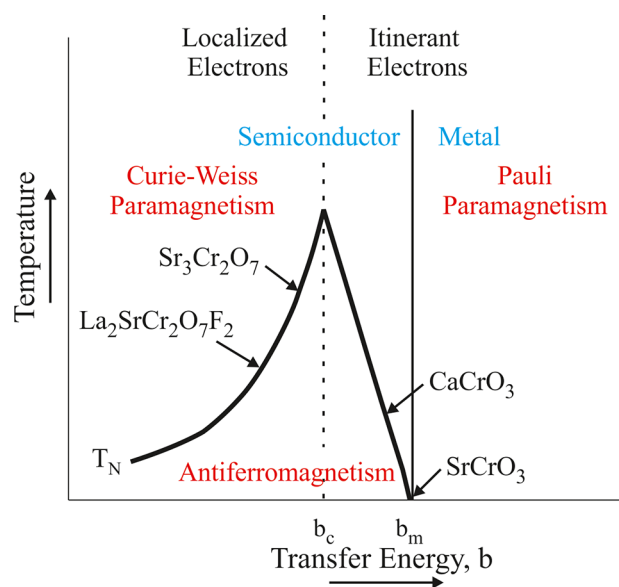


**Figure 5.** Schematic plot of the temperature-transfer integral phase diagram for one electron per orbital. Arrows indicate apparent positions of Cr<sup>4+</sup> phases.

shows a schematic phase diagram for the expected evolution of the magnetic ordering temperature (*T*<sub>N</sub>) of a phase as a function of interaction strength. When the interaction between metal centers is low (small *b*), phases are highly insulating with low magnetic ordering temperatures. As *b* increases, superexchange interactions strengthen and *T*<sub>N</sub> increases. However, when the interaction between metals reaches a critical value, *b*<sub>*c*</sub>, intermetallic interactions are strong enough to allow some of the valence electrons to become itinerant, screening the

magnetic couplings between neighboring metal centers, weakening the superexchange interactions and leading to a decline in  $T_N$  with increasing  $b$ , until metallic behavior and Pauli paramagnetism are observed at  $b_m$ .

The perovskite phases  $\text{CaCrO}_3$  and  $\text{SrCrO}_3$  are thought to lie close to metallic behavior in the range  $b_c < b < b_m$ . In this region the structural distortion observed for  $\text{CaCrO}_3$  would result in a weakening of the intermetallic interaction (smaller  $b$ ) in comparison to undistorted  $\text{SrCrO}_3$ , consistent with the larger  $T_N$  value observed for the calcium phase, as shown in Figure 5. In contrast, the layered phases  $\text{Sr}_3\text{Cr}_2\text{O}_7$  and  $\text{La}_2\text{SrCr}_2\text{O}_7\text{F}_2$  appear to lie in the region  $b < b_c$ , as this would be consistent with the observation that  $T_N$  declines with decreasing Cr–O–Cr bond angle. The small transfer integral,  $b$ , observed for the layered Ruddlesden–Popper phases in comparison to that for the perovskite materials can be rationalized by observing that the addition of rock salt layers into the extended perovskite lattice lowers the dimensionality of the system, decreasing the average Cr–Cr intercation interaction and thus reducing  $b$ . An analogous band narrowing has been observed in the  $\text{Sr}_{n+1}\text{Ir}_n\text{O}_{3n+1}$  series, in which “3-dimensional”  $\text{SrIrO}_3$  is a correlated metal but “2-dimensional”  $\text{Sr}_2\text{IrO}_4$  is a Mott insulator.<sup>22</sup>

## CONCLUSION

Topochemical fluorination of  $\text{La}_2\text{SrCr}_2\text{O}_7$  to  $\text{La}_2\text{SrCr}_2\text{O}_7\text{F}_2$  demonstrates that low-temperature, structure-conserving oxidation reactions can be used to prepare phases containing arrays of apex-linked  $\text{Cr}^{4+}\text{O}_6$  units, at ambient pressure. The observation of robust antiferromagnetic order below  $T_N \approx 140$  K in  $\text{La}_2\text{SrCr}_2\text{O}_7\text{F}_2$  suggests that the presence of the La/Sr–O–F layers between the perovskite blocks lowers that average Cr–Cr intercation interaction and as a result the oxy-fluoride phase lies further from the crossover for insulating to metallic behavior in comparison to many other  $\text{Cr}^{4+}$  oxide phases.

## ASSOCIATED CONTENT

### Supporting Information

The Supporting Information is available free of charge on the ACS Publications website at DOI: 10.1021/acs.inorgchem.6b00114.

Thermogravimetric data from the reduction of  $\text{La}_2\text{SrCr}_2\text{O}_7\text{F}_2$ , X-ray powder diffraction data from the TGA reduction of  $\text{La}_2\text{SrCr}_2\text{O}_7\text{F}_2$ , structural details of  $\text{La}_2\text{SrCr}_2\text{O}_7$ , observed and calculated diffraction data from the structural and magnetic refinement of  $\text{La}_2\text{SrCr}_2\text{O}_7\text{F}_2$  at 300 and 5 K, complete details of the 5 K structural and magnetic refinement of  $\text{La}_2\text{SrCr}_2\text{O}_7\text{F}_2$ , and plots of  $\mu^+\text{SR}$  asymmetry against time at 10 and 130 K (PDF)

## AUTHOR INFORMATION

### Corresponding Author

\*M.A.H.: tel, +44 1865 272623; fax, +44 1865 272690; e-mail, michael.hayward@chem.ox.ac.uk.

### Author Contributions

The manuscript was written through contributions of all authors.

### Notes

The authors declare no competing financial interest.

## ACKNOWLEDGMENTS

We thank W. Kockelmann and I. da Silva for assistance in collecting the neutron powder diffraction data. Experiments at the ISIS pulsed neutron facility were supported by a beam time allocation from the Science and Technology Facilities Council. Part of this work was carried out at the Swiss muon source  $\text{S}\mu\text{S}$ , Paul Scherrer Institut, Villigen, Switzerland. Part of this work was supported by the EPSRC (EP/M020517/1).

## REFERENCES

- (1) Goodenough, J. B. *Localized to Itinerant Electronic Transition in Perovskite Oxides*; Springer-Verlag: Berlin, 2001.
- (2) Castillo-Martinez, E.; Alario-Franco, M. A. *Solid State Sci.* **2007**, *9*, 564–573.
- (3) Hayward, M. A. In *Comprehensive Inorganic Chemistry II*; Reedijk, J., Poeppelmeier, K. R., Eds.; Elsevier: Oxford, U.K., 2013; Vol. 2, pp 417–453.
- (4) Hayward, M. A. *Semicond. Sci. Technol.* **2014**, *29*, 064010.
- (5) Romero, F. D.; Bingham, P. A.; Forder, S. D.; Hayward, M. A. *Inorg. Chem.* **2013**, *52*, 3388.
- (6) Li, R. K.; Greaves, C. *Phys. Rev. B: Condens. Matter Mater. Phys.* **2000**, *62*, 3811–3815.
- (7) Sivakumar, T.; Wiley, J. B. *Mater. Res. Bull.* **2009**, *44*, 74–77.
- (8) Zhang, R.; Read, G.; Benedek, N. A.; Hayward, M. A. Manuscript in preparation.
- (9) Luo, K.; Tran, T. T.; Halasyamani, P. S.; Hayward, M. A. *Inorg. Chem.* **2013**, *52*, 13762.
- (10) Larson, A. C.; Von Dreele, R. B. *Los Alamos National Laboratory Report LAUR 86-748*, 2000.
- (11) Sears, V. F. *Neutron News* **1992**, *3*, 26–37.
- (12) Brese, N. E.; O’Keeffe, M. *Acta Crystallogr., Sect. B: Struct. Sci.* **1991**, *47*, 192–197.
- (13) Wills, A. S. *Phys. B* **2000**, *276-278*, 680–681.
- (14) Case, G. S.; Hector, A. L.; Levason, W.; Needs, R. L.; Thomas, M. F.; Weller, M. T. *J. Mater. Chem.* **1999**, *9*, 2821–2827.
- (15) Greis, O.; Petzel, T. Z. *Anorg. Allg. Chem.* **1974**, *403*, 1–22.
- (16) Glazer, A. M. *Acta Crystallogr., Sect. B: Struct. Crystallogr. Cryst. Chem.* **1972**, *28*, 3384.
- (17) Goodenough, J. B.; Longo, J. M.; Kafalas, J. A. *Mater. Res. Bull.* **1968**, *3*, 471.
- (18) Castillo-Martinez, E.; Duran, A.; Alario-Franco, M. A. *J. Solid State Chem.* **2008**, *181*, 895–904.
- (19) Zhou, J. S.; Jin, C. Q.; Long, Y. W.; Yang, L. X.; Goodenough, J. B. *Phys. Rev. Lett.* **2006**, *96*, 046408.
- (20) Ortega-San-Martin, L.; Williams, A. J.; Rodgers, J.; Attfield, J. P.; Heymann, G.; Huppertz, H. *Phys. Rev. Lett.* **2007**, *99*, 255701.
- (21) Battle, P. D.; Goodenough, J. B.; Price, R. J. *Solid State Chem.* **1983**, *46*, 234–244.
- (22) Moon, S. J.; Jin, H.; Kim, K. W.; Choi, W. S.; Lee, Y. S.; Yu, J.; Cao, G.; Sumi, A.; Funakubo, H.; Bernhard, C.; Noh, T. W. *Phys. Rev. Lett.* **2008**, *101*, 226402.